Materials Advances

ROYAL SOCIETY OF CHEMISTRY

PAPER

A guanidine-functionalized graphene oxide/Fe$_3$O$_4$ nanocomposite as a magnetically recoverable heterogeneous catalyst for the Hantzsch reaction

Akram Rahro, Alireza Salimi Beni [ID] * and Somayeh Abaeezadeh

In this study, a guanidine-functionalized graphene oxide/Fe$_3$O$_4$ nanocomposite (Gu-GO/Fe$_3$O$_4$) was synthesized and demonstrated as an efficient and magnetically recoverable catalyst for the synthesis of polyhydroquinoline derivatives *via* the unsymmetrical Hantzsch reaction under mild conditions. The catalyst was produced by the covalent immobilization of guanidine onto a 3-chloropropyl triethoxysilane-modified graphene/Fe$_3$O$_4$ support. The synthesized Gu-GO/Fe$_3$O$_4$ nanocatalyst was characterized using FT-IR, SEM, VSM, XRD, and TGA. Optimization studies for the unsymmetrical Hantzsch reaction revealed that 0.005 g of Gu-GO/Fe$_3$O$_4$ at 50 °C under solvent-free conditions afforded good to excellent product yields. The catalyst exhibited facile magnetic recovery using an external magnet and retained its catalytic activity and structural integrity after nine reuse cycles. A hot-filtration experiment confirmed the heterogeneous nature of the catalytic system.

1. Introduction

Nanomaterials have attracted significant attention in recent years.[1–5] These materials have attracted attention due to their exceptional physicochemical properties,[6] especially their high surface-to-volume ratio.[7] These characteristics make them highly effective in catalytic applications, where they can significantly enhance reaction rates and selectivity.[8]

The development of efficient, environmentally friendly, and reusable catalytic systems is a key focus in sustainable chemistry.[9,10] In recent years, heterogeneous catalysis has gained significant attention due to its advantages, such as ease of separation, recovery, and potential for reuse.[11–19] Heterogeneous catalysis plays a critical role in numerous scientific and industrial sectors, including the chemical and pharmaceutical industries, energy conversion technologies, environmental remediation, and materials science. Within this field, supported catalysts represent a dominant class.[20] Among the diverse supports used in heterogeneous catalysis, carbon-based materials have garnered increasing attention due to their unique properties. The large surface area of these materials enables high loading of active sites, while their chemical stability allows them to resist degradation under both acidic and basic conditions. Also, high thermal stability, low cost and hydrophobic nature are other advantages of these materials.[20–23] Several types of carbon materials have been

investigated as catalyst supports, including pyrolytic carbon, activated carbon, glassy carbon, carbon black, polymer-derived carbon, carbon nanotubes, graphene, fullerene, mesoporous carbons and their derivatives. These materials exhibit varying structural and textural properties that can influence the overall performance of the resulting catalysts.[22] Graphene oxide (GO) exhibits unique properties compared to other carbon supports. Its two-dimensional structure, high mechanical and thermal stability, large active surface area, well-developed porosity and excellent electronic properties make it a key material in heterogeneous catalyst systems. Furthermore, the presence of abundant surface functional groups, such as carboxylic acid, carbonyl, hydroxyl, and epoxide, enables covalent attachment to specific groups, making GO a versatile support.[20,23–25] While the dispersion of GO nanosheets in the solution medium is generally high, their effective separation from the solution medium presents a significant challenge. Traditional separation techniques such as centrifugation or filtration are often inefficient and time-consuming due to the strong inter-sheet interactions and the colloidal stability of the GO nanosheets in the solution. To facilitate post-reaction separation, the development of magnetic graphene nanocomposites is a promising strategy.[26–33] The incorporation of Fe$_3$O$_4$ nanoparticles onto the GO surface improves the overall separation capability of the nanocomposite. This enhanced separation efficiency contributes to the sustainability and cost-effectiveness of the catalytic process, making magnetic graphene nanocomposites an attractive option for a wide range of applications in heterogeneous catalysis.[34–38] Some reports in this matter are

Department of Chemistry, Faculty of Science, Yasouj University, 75918-74831, Yasouj, Iran. E-mail: salimibeni@yu.ac.ir, alirezasalimi7173291@gmail.com

Fe$_3$O$_4$@GO–Pr–SO$_3$H,[34] Fe$_3$O$_4$@GO,[35] GO–Fe$_3$O$_4$–Au NPs(G),[36] N-RGO/Fe$_3$O$_4$,[37] NaOH@GO–Fe$_3$O$_4$,[38] GO/Fe$_3$O$_4$@PDA/Pd[39] and MGO–NH$_2$.[40]

On the other hand, polyhydroquinolines (PHQs) are a vital class of heterocyclic compounds known for their diverse biological and pharmacological activities, encompassing anti-malarial, anti-inflammatory, anti-cancer, and anti-diabetic properties. This broad spectrum of applications has fueled considerable research into developing efficient and versatile synthetic routes for their pre-paration. The utilization of both homogeneous and heterogeneous catalysts has been explored to improve the efficiency and sustain-ability of the Hantzsch reaction. Homogeneous catalysts, such as transition metal complexes and organocatalysts, have demon-strated high catalytic activity and selectivity. However, their

separation from the reaction mixture and recycling remains challenging. On the other hand, heterogeneous catalysts give benefits such as simplicity of separation, recovery, and reusability. Various heterogeneous catalytic systems, including metal–organic frameworks, functionalized graphene oxide, and magnetic nano-particles, have been investigated for the Hantzsch reaction.[41–57] In light of the importance of expanding effective catalytic methods for the production of polyhydroquinolines, a novel guanidine-functionalized graphene oxide/Fe$_3$O$_4$ nanocomposite (Gu-GO/Fe$_3$O$_4$) has been designed and synthesized. The catalytic perfor-mance of this composite material is investigated for the synthesis of polyhydroquinoline derivatives *via* the unsymmetrical Hantzsch reaction.
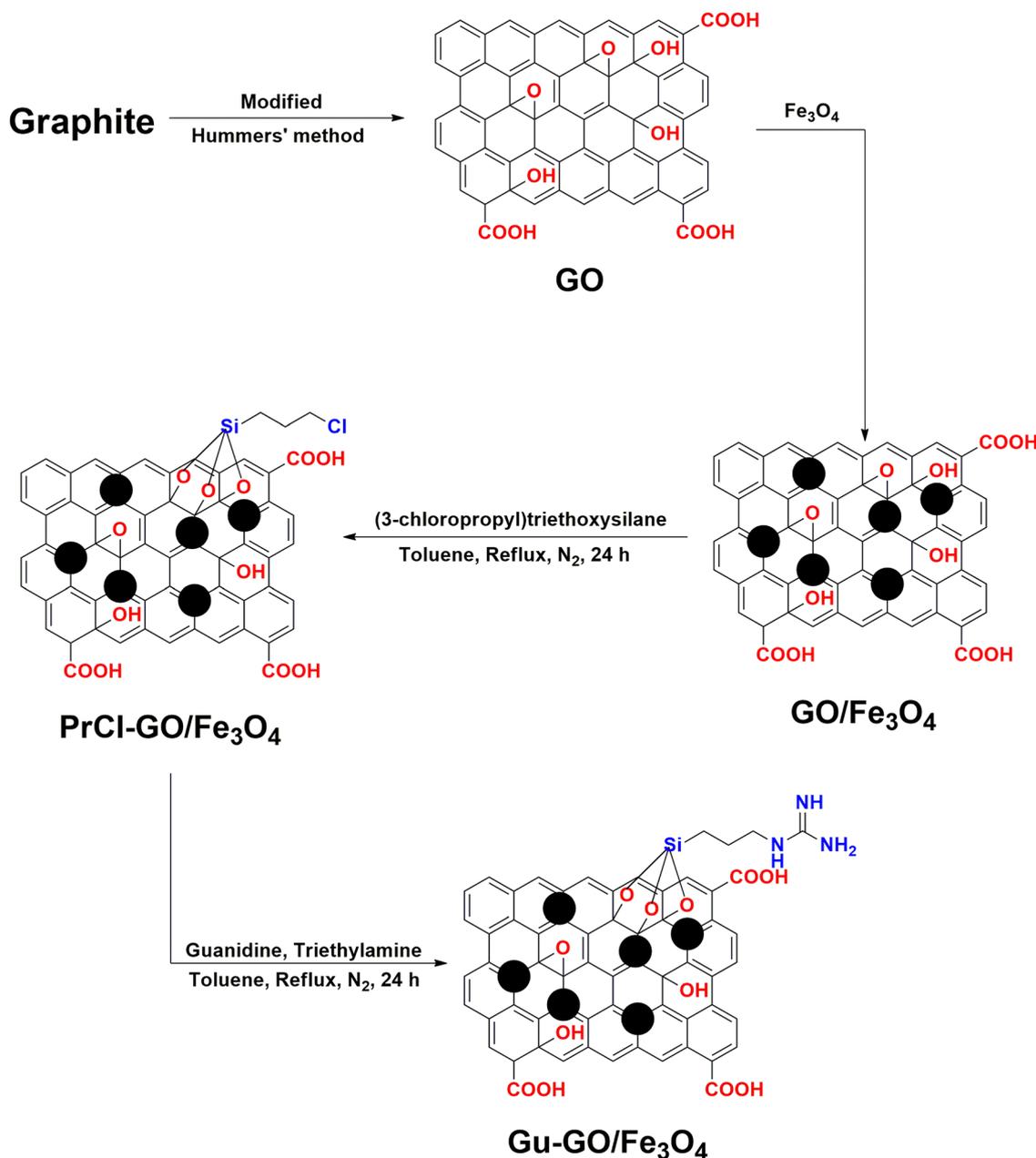
Scheme 1 Synthesis of Gu-GO/Fe$_3$O$_4$.

2. Experimental section

2.1. Synthesis of Gu-GO/Fe₃O₄

2.1.1. Synthesis of GO. Graphene oxide (GO) was synthesized according to the Hummers' method. In the initial stage, 10 g graphite powder (<20 μm, synthetic, Sigma-Aldrich) was introduced into a 1000 mL reaction vessel, which was placed in an ice-water bath under continuous stirring. Subsequently, sodium nitrate (0.75 g) was added to the graphite, followed by the slow addition of sulfuric acid (75 mL, 98%). Following this, potassium permanganate (KMnO₄, 5.4 g) was incorporated into the mixture as an oxidizing agent. The reaction vessel was then sealed with Parafilm and maintained at room temperature for a period of 5 days. After this period, sulfuric acid (7 mL, 98%) and deionized water (140 mL) were carefully added, resulting in a color change to dark green. Subsequently, sulfuric acid (200 mL, 3%) and hydrogen peroxide (H_2O_2 5%, 3 mL) were added to the reaction mixture, which was then subjected to sonication for approximately 30 min. To neutralize the reaction mixture, it was centrifuged for a minimum of 24 h. The resulting precipitate was transferred onto watch glasses and allowed to dry at ambient temperature for 24 h. Following desiccation, the dried precipitate was transferred to a mortar and thoroughly ground.

2.1.2. Synthesis of Fe₃O₄ NPs. For this aim, a solution was prepared by dissolving $FeCl_2 \cdot 4H_2O$ (2 g) and $FeCl_3 \cdot 6H_2O$ (5.2 g) in HCl solution (1 N, 25 mL). Subsequently, NaOH solution (1.5 M, 250 mL) was added dropwise over 20 min under a N_2 atmosphere at a controlled temperature of 80 °C (the reaction temperature was kept constant at 80 °C by using an oil bath at 80 °C, the temperature of which was previously adjusted by a heater-stirrer device) and the reaction mixture was stirred at 1000 rpm. The resulting black precipitate was magnetically separated, washed repeatedly with deionized water, and dried at 40 °C.

Table 1 The CHNS analysis of the Gu-GO/Fe₃O₄ nanocomposite

Component name	Element (%)
Nitrogen	6.79
Carbon	27.63
Hydrogen	2.23
Sulphur	0.00

2.1.3. Synthesis of GO/Fe₃O₄. In a reaction vessel, previously synthesized Fe₃O₄ (2 g) was combined with distilled water (100 mL) and EtOH (200 mL). The mixture was then sonicated for 10 min to ensure proper dispersion of the particles. Subsequently, GO (1.5 g) was introduced into the mixture, followed by an additional 15 min of sonication to achieve homogenous dispersion. The resulting mixture was stirred for 24 h at room temperature. Following the reaction, the GO/Fe₃O₄ composite was separated using an external magnet. The composite was then washed with deionized water to remove any residual impurities and dried at 50 °C.

2.1.4. Synthesis of Gu-GO/Fe₃O₄. For this, GO/Fe₃O₄ (1.0 g) was dispersed in 50 mL of dried toluene in an ultrasonic bath for 15 min. Subsequently, (3-chloropropyl)triethoxysilane (1 mL) was added to the mixture under a N_2 atmosphere, and the reaction was refluxed for 24 h. After that, the resulting materials were separated using an external magnet, washed with H_2O and EtOH, dried at 80 °C and called PrCl–GO/Fe₃O₄. In the next step, PrCl–GO/Fe₃O₄ (1.5 g) was added into a reaction vessel containing dried toluene (75 mL) and dispersed for 10 min. Then, guanidine (0.5 g) and triethylamine (0.02 mL) were added to the mixture and refluxed for 24 h. The obtained materials were subsequently washed with EtOH and dried in an oven at 70 °C and called Gu-GO/Fe₃O₄.

2.2. Synthesis of polyhydroquinolines in the presence of the Gu-GO/Fe₃O₄ nanocatalyst

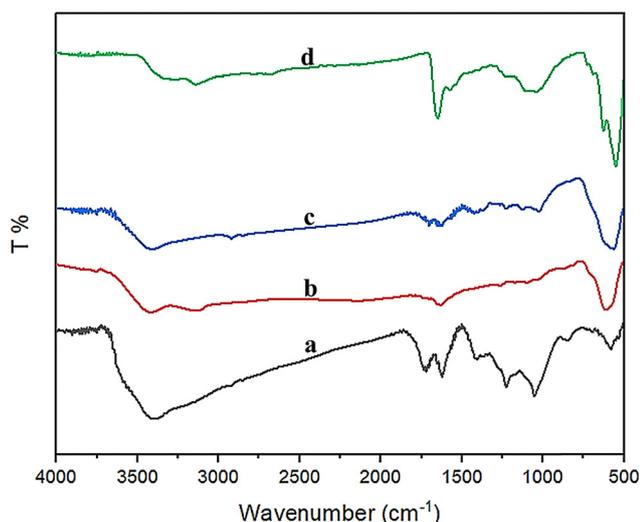A reaction vessel was charged with benzaldehyde (1 mmol), dimedone (1 mmol), ethyl acetoacetate (1 mmol), ammonium

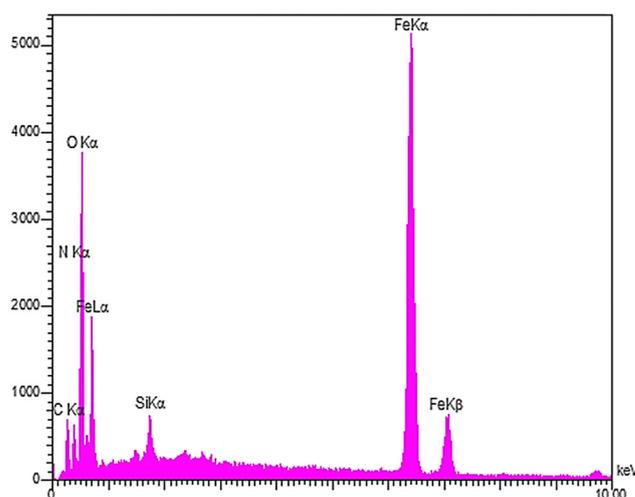**Fig. 1** FT-IR spectra of (a) GO, (b) Fe₃O₄, (c) GO/Fe₃O₄ and (d) Gu-GO/Fe₃O₄.

Fig. 2 EDX analysis of the Gu-GO/Fe₃O₄ nanocomposite.

acetate (1.4 mmol), and Gu-GO/Fe₃O₄ nanocatalyst (5 mg). The resulting mixture was stirred under solvent-free conditions at 50 °C. The reaction progress was monitored by TLC. Upon the end of the reaction, 10 mL of hot EtOH was added to the reaction mixture. The Gu-GO/Fe₃O₄ catalyst was efficiently removed from the solution using an external magnet. The solvent was subsequently evaporated, and the raw products were recrystallized from EtOH to get the pure product.

3. Results and discussion

The synthesis of the Gu-GO/Fe₃O₄ nanocomposite is shown in Scheme 1. First, graphene oxide (GO) was synthesized according to the Hummers' method. Then, Fe₃O₄ was chemically immobilized on the surface of GO. After that, the surface of GO/Fe₃O₄ was chemically modified with (3-chloropropyl)triethoxysilane to give the PrCl–GO/Fe₃O₄ nanocomposite. Finally, the guanidine was covalently immobilized onto the PrCl–GO/Fe₃O₄ support. In the next step, the chemical and physical properties of the synthesised nanocomposite were studied by using various techniques.

FT-IR spectra of GO, Fe₃O₄, GO/Fe₃O₄ and Gu-GO/Fe₃O₄ are depicted in Fig. 1. For all samples, the strong peak at ~ 3400 cm^{-1} is due to the O–H bonds of the material surface. Moreover, the peaks at 1730, 1621, 1230 and 1051 cm^{-1} are, respectively, associated with the C=O stretching vibration of the carboxylic acid group, stretching vibration mode of the C=C bond and C–O stretching of phenolic and epoxy groups of GO nanosheets (Fig. 1a–d).[31] For Gu-GO/Fe₃O₄, the stretching
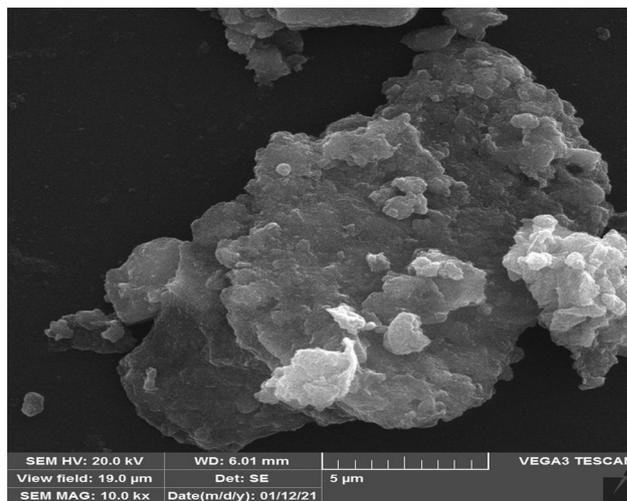

Fig. 4 SEM image of the Gu-GO/Fe₃O₄ nanocomposite.

vibration at 1668 cm^{-1} related to C=N proved the presence of guanidine at the surface of the GO/Fe₃O₄ nanocomposite (Fig. 1d).[58] For the Fe₃O₄, GO/Fe₃O₄ and Gu-GO/Fe₃O₄ materials, the peak observed at 588 cm^{-1} is related to the stretching vibrations of the Fe–O bond, which confirms the successful formation of Fe₃O₄ and its stability during the synthesis of the Gu-GO/Fe₃O₄ nanocatalysts (Fig. 1b–d).[12]

Although FT-IR spectroscopy confirmed the presence of propylguanidine groups, CHNS elemental analysis was employed to quantitatively evaluate the amount of propylguanidine
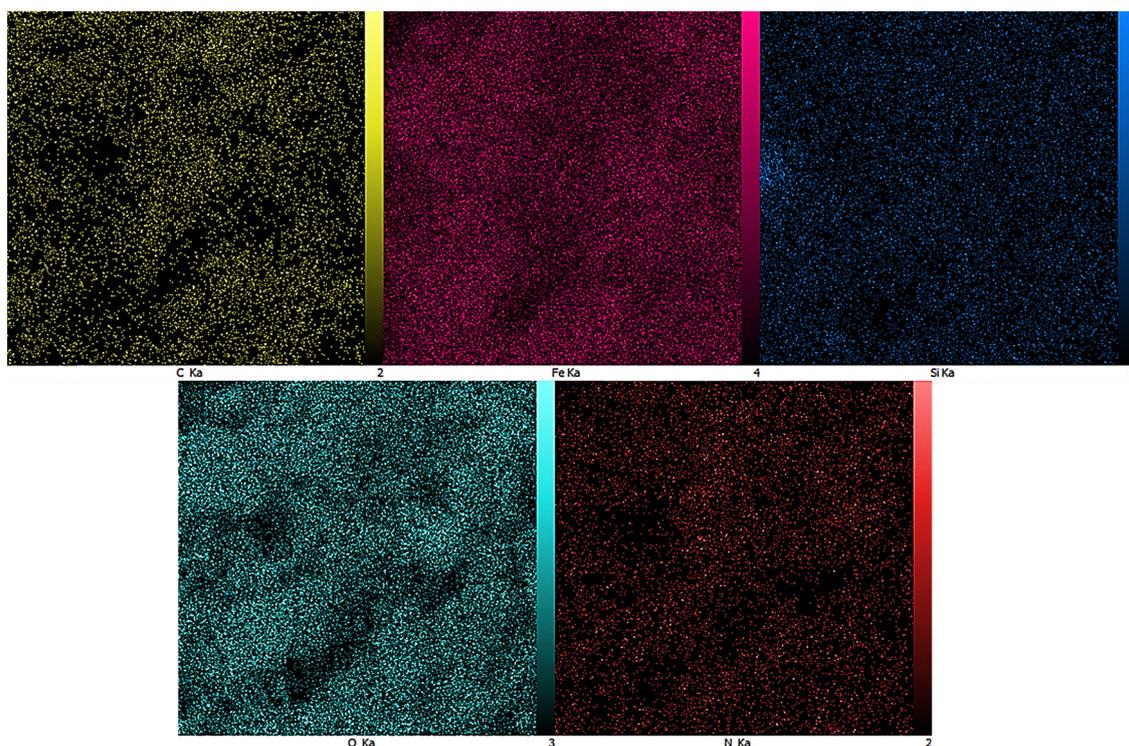

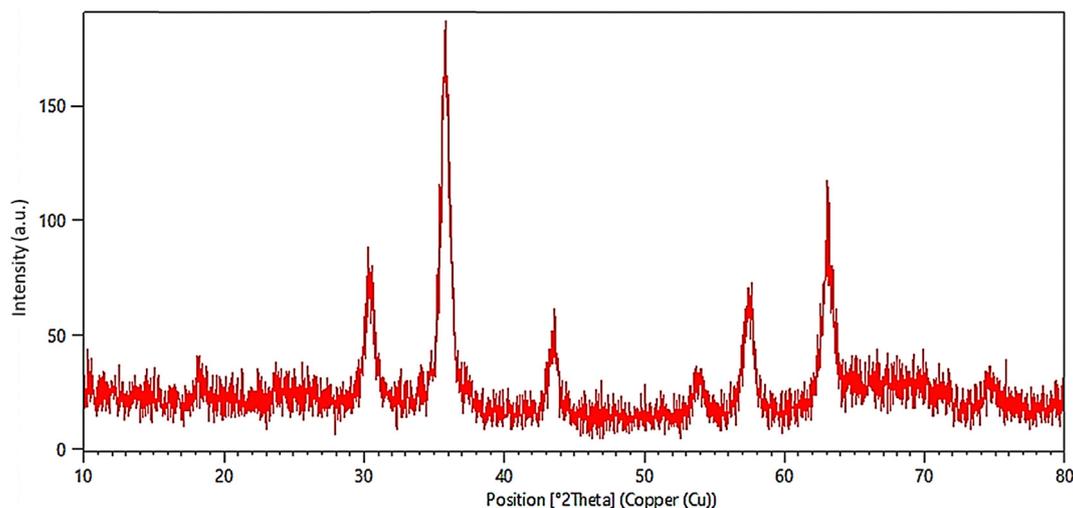Fig. 3 EDX mapping analysis of the Gu-GO/Fe₃O₄ nanocomposite.

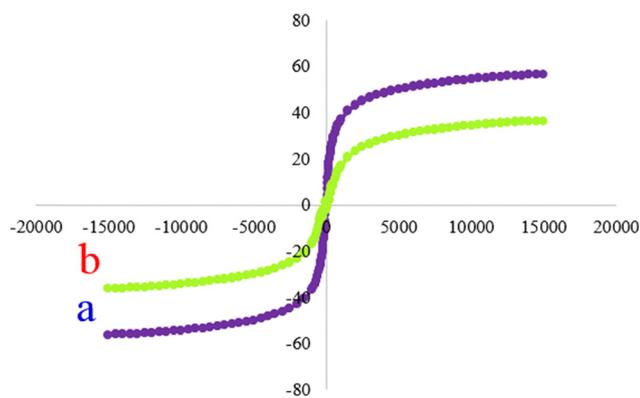**Fig. 5** XRD pattern of the Gu-GO/Fe$_3$O$_4$ nanocomposite.

Fig. 6 VSM diagrams of the (a) Fe$_3$O$_4$ and (b) Gu-GO/Fe$_3$O$_4$ nanocomposite.

functionalized onto the GO/Fe$_3$O$_4$ surface. According to the results summarized in Table 1, the successful incorporation of propylguanidine moieties was evidenced by the measured elemental

Fig. 7 Magnetic separation ability of the Gu-GO/Fe$_3$O$_4$ nanocomposite.

Table 2 Evaluation of the magnetic properties of the Gu-GO/Fe$_3$O$_4$ nanocomposite in comparison with previously reported magnetic nanomaterials

Magnetic composites	MS (emu g^{-1})	Ref.
Pt-APA@Fe$_3$O$_4$/GO	31.7	60
Fe$_3$O$_4$/GO@melamine-ZnO	17	61
GO/Fe$_3$O$_4$@Dop/Au	42.2	62
Ag$_3$PO$_4$/Fe$_3$O$_4$/GO	2.28	63
GO@Fe$_3$O$_4$	0.22	64
Gu-GO/Fe$_3$O$_4$	30	This work

contents: 6.79% nitrogen, 27.63% carbon, and 2.23% hydrogen. These values clearly indicate the effective surface modification of the GO/Fe$_3$O$_4$ nanocomposite with propylguanidine functionalities.

The elemental composition of the Gu-GO/Fe$_3$O$_4$ nanocomposite was determined using EDX spectroscopy (Fig. 2). The EDX spectrum confirmed the presence of C, O, Si, N, and Fe, elements consistent with the expected composition based on the synthesis scheme (Scheme 1). Furthermore, EDX mapping (Fig. 3) demonstrated a uniform distribution of these elements throughout the nanocomposite structure.

The surface morphology of the Gu-GO/Fe$_3$O$_4$ nanocomposite was investigated using SEM. It should be noted that for SEM analysis, the Gu-GO/Fe$_3$O$_4$ nanocomposite was coated with gold and the accelerating voltage for this analysis was 20 kV. As can be seen in Fig. 4, the SEM image revealed the presence of spherical Fe$_3$O$_4$ nanoparticles and the characteristic layered structure of GO.

The XRD pattern of the Gu-GO/Fe$_3$O$_4$ nanocomposite (Fig. 5) exhibited six diffraction peaks at 2θ values of 30°, 36°, 44°, 54°, 57°, and 63°, which correspond to the (220), (311), (400), (422), (511), and (440) crystallographic planes of Fe$_3$O$_4$, respectively. These peaks confirm the presence of a spinel structure, indicating that the magnetite nanoparticles maintained their structural integrity throughout the modification process.[29] Although a

Paper

Materials Advances
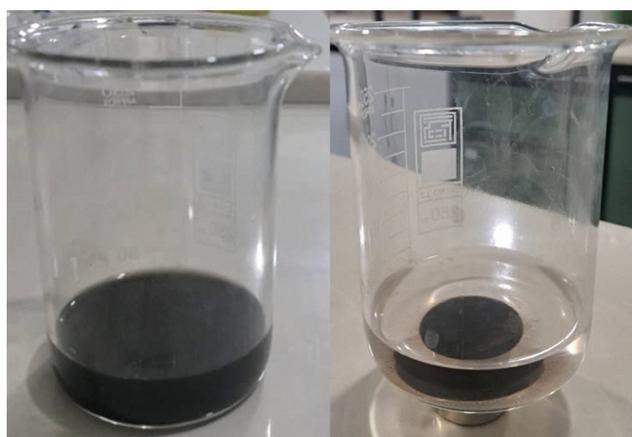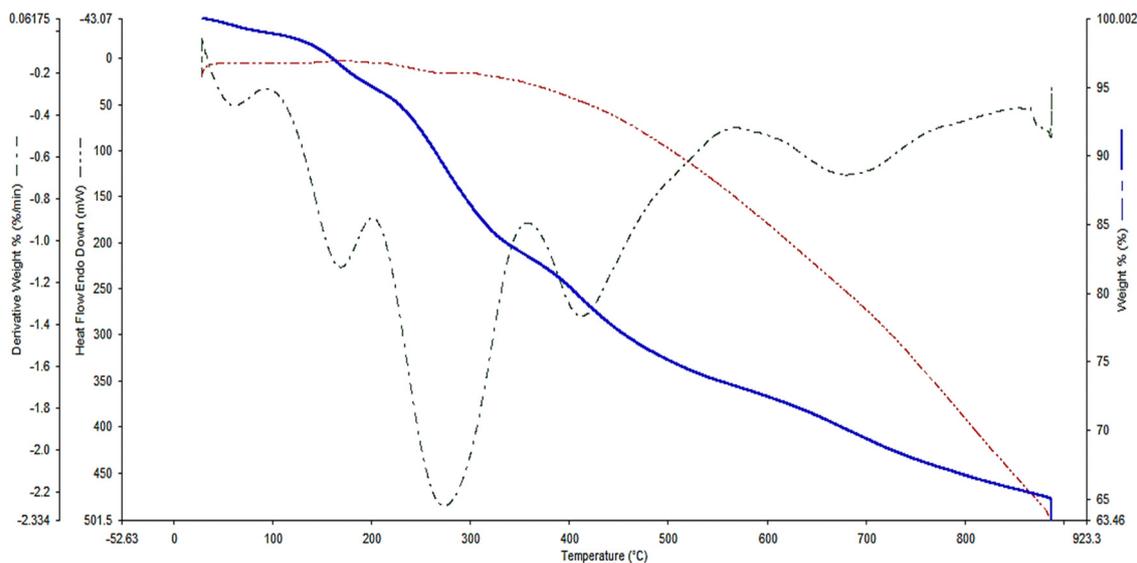
Fig. 8 TGA analysis of the Gu-GO/Fe$_3$O$_4$ nanocomposite.

characteristic diffraction peak of graphene oxide (GO) is typically observed at approximately $2\theta = 11°$, no such peak is detected in the XRD pattern of the synthesized Gu-GO/Fe$_3$O$_4$ nanocomposite. This absence suggests that the stacking of GO sheets has been effectively disrupted by the loading of Fe$_3$O$_4$ nanoparticles.[35,59]

The magnetic properties of the Fe$_3$O$_4$ and Gu-GO/Fe$_3$O$_4$ nanomaterials were characterized using VSM. Analysis revealed superparamagnetic behavior in all samples, as evidenced by the absence of hysteresis, remanence, and coercivity. The saturation magnetization of Fe$_3$O$_4$ was determined to be 60 emu g^{-1}, while the Gu-GO/Fe$_3$O$_4$ nanocomposite exhibited a lower saturation

magnetization of 30 emu g^{-1}. This reduction in saturation magnetization is consistent with the successful chemical immobilization of Fe$_3$O$_4$ nanoparticles onto the GO surface (Fig. 6). Fig. 7 illustrates the prompt and efficient magnetic separation capability of the Gu-GO/Fe$_3$O$_4$ nanocomposite, enabled by its strong response to an external magnetic field. This behavior underscores its potential for facile recovery and reusability in chemical processes.

To further evaluate the magnetic performance of the synthesized Gu-GO/Fe$_3$O$_4$ nanocomposite, its magnetic behavior was evaluated in comparison with previously reported magnetic

Table 3 Optimization of the reaction conditions for the synthesis of polyhydroquinolines by Gu-GO/Fe$_3$O$_4$

Entry	Catalyst (mg)	Solvent	T (°C)	Time (min)	Yield^a (%)
1	—	—	50	20	Trace
2	1	—	50	20	87
3	3	—	50	20	90
4	**5**	**—**	**50**	**20**	**98**
5	8	—	50	20	98
6	5	—	RT	20	62
7	5	—	40	20	80
8	5	—	60	20	98
9	5	Toluene	50	20	32
10	5	Acetonitrile	50	20	73
11	5	EtOH	50	20	85
12	GO (5 mg)	—	50	20	65
13	Fe$_3$O$_4$ (5 mg)	—	50	20	80
14	GO/Fe$_3$O$_4$ (5 mg)	—	50	20	81
15	Guanidine (5 mg)	—	50	20	85

^{a} Isolated yields.

Table 4 Production of polyhydroquinoline derivatives by the Gu-GO/Fe$_3$O$_4$ catalyst

Entry	Aldehyde	Product	Time (min)	Yield[a] (%)	M.P. (°C) found	M.P. (°C) reported
1			20	98	204–206	203–207[41]
2			15	97	238–240	237–239[41]
3			10	99	145–143	147–149[41]
4			12	96	252–254	254–256[41]
5			15	95	250–252	250–252[41]
6			10	97	199–201	197–199[67]

Table 4 (continued)
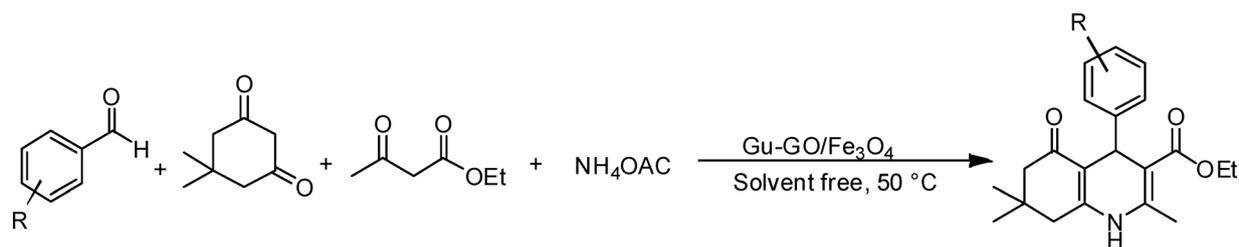
Entry	Aldehyde	Product	Time (min)	Yield[a] (%)	M.P. (°C) found	M.P. (°C) reported
7			10	97	263–265	261–263[41]
8			12	97	239–241	241–243[41]
9			15	95	206–208	206–208[41]
10			13	96	243–245	244–246[41]
11			15	93	240–242	243–245[68]
12			13	93	219–221	218–220[68]

[a] Isolated yields.

Fig. 9 Reusability of the Gu-GO/Fe$_3$O$_4$ nanocatalyst.

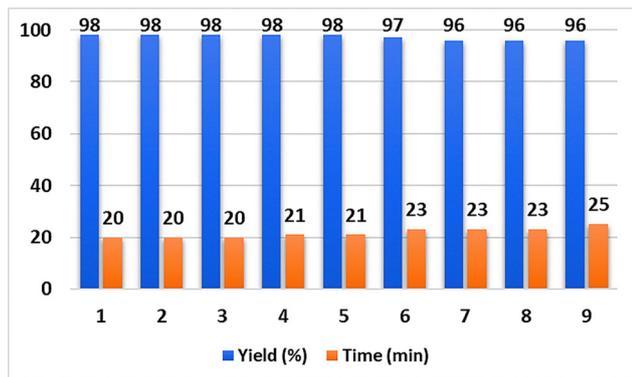catalysts (Table 2). The findings revealed that this nanocomposite exhibits superior or at least comparable magnetic response, which supports its efficient separation by external magnetic fields, highlighting its application in catalytic and separation processes.

Thermogravimetric analysis (TGA) was used to assess the thermal stability of the Gu-GO/Fe$_3$O$_4$ nanocomposite across a temperature range of 25–900 °C. The resultant TGA thermogram (Fig. 8) reveals distinct mass loss events indicative of the composite's thermal decomposition profile. An initial mass loss of 2% observed between 25 and 100 °C is attributed to the volatilization of adsorbed solvent molecules. A subsequent 2% mass loss between 100 and 210 °C corresponds to the degradation of thermally labile oxygen-containing functional groups (e.g., hydroxyl, epoxy, and carboxylic acid moieties). A more substantial 9% mass loss between 210 and 350 °C is

Fig. 10 The SEM image of the recovered Gu-GO/Fe$_3$O$_4$ catalyst.

associated with the decomposition of more thermally stable oxygen-containing functionalities and the bulk pyrolysis of the carbonaceous framework. The most prominent mass loss of approximately 10% occurring between 350 and 580 °C is assigned to the decomposition of the propyl-guanidine moieties supported on the GO/Fe$_3$O$_4$ surface. This observation suggests a strong chemical interaction between the GO/Fe$_3$O$_4$ nanocomposite and the propyl-guanidine groups.[28] Additionally, this observation is consistent with the elemental CHNS analysis, further confirming the successful functionalization of the nanocomposite with propyl-guanidine.

Following characterization, the catalytic activity of the Gu-GO/Fe$_3$O$_4$ composite was evaluated in a model one-pot Hantzsch condensation reaction. This reaction involved benzaldehyde (1 mmol), dimedone (1 mmol), ethyl acetoacetate (1 mmol), and ammonium acetate (1.4 mmol). Optimization of the reaction conditions was performed by varying parameters such as catalyst loading, solvent, and temperature (Table 3).

Investigation of catalyst loading revealed a strong dependence of reaction progression on catalyst quantity (Table 3, entries 1–5). In the absence of the catalyst, only trace amounts of product were observed (Table 3, entry 1), indicating its essential role. Optimal product yield was achieved with a catalyst loading of 5 mg of Gu-GO/Fe$_3$O$_4$ (Table 3, entry 4). As presented in Table 3, entry 5, increasing the catalyst loading to 8 mg did not increase the reaction efficiency. This observation is likely attributed to mass transfer limitations that become more pronounced at higher catalyst concentrations, especially when the catalyst is in a heterogeneous phase with respect to the reactants. Under such conditions, excess catalyst may lead to aggregation or reduced diffusion of reactants to the catalytic active sites, thereby impairing the overall catalyst performance.[65]

The reaction temperature was subsequently optimized, with 50 °C identified as the most effective (Table 3, entry 4 vs. entries 6–8). Solvent optimization studies were conducted using ethanol, acetonitrile, toluene, and a solvent-free system. The highest product yield was obtained after 20 minutes under solvent-free conditions (Table 3, entry 4 vs. entries 9–11). It should be noted that organic solvents are often volatile, flammable, and toxic. Therefore, performing the reaction under solvent-free conditions aligns with green chemistry principles by eliminating the use of volatile organic solvents, thereby reducing environmental pollution and hazardous waste. It also improves energy efficiency and process safety.[66]

To ascertain the specific contribution of the guanidine moieties to the catalytic process, control experiments were performed using guanidine-free GO, Fe$_3$O$_4$, and GO/Fe$_3$O$_4$ nanomaterials. These materials exhibited negligible catalytic activity under the optimized conditions and reaction time employed with the Gu-GO/Fe$_3$O$_4$ catalyst (Table 3, entry 4 vs. entries 12–14). These results unequivocally demonstrate the critical role of the guanidine functionalities as the catalytic centers in this reaction.

To further validate the contribution of the support in catalytic performance, a control experiment using free guanidine (5 mg) under the same conditions was conducted. The reaction proceeded
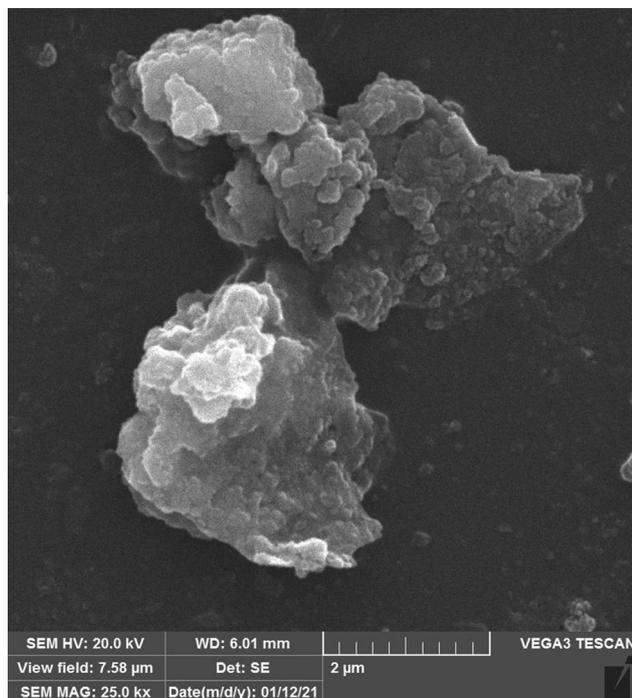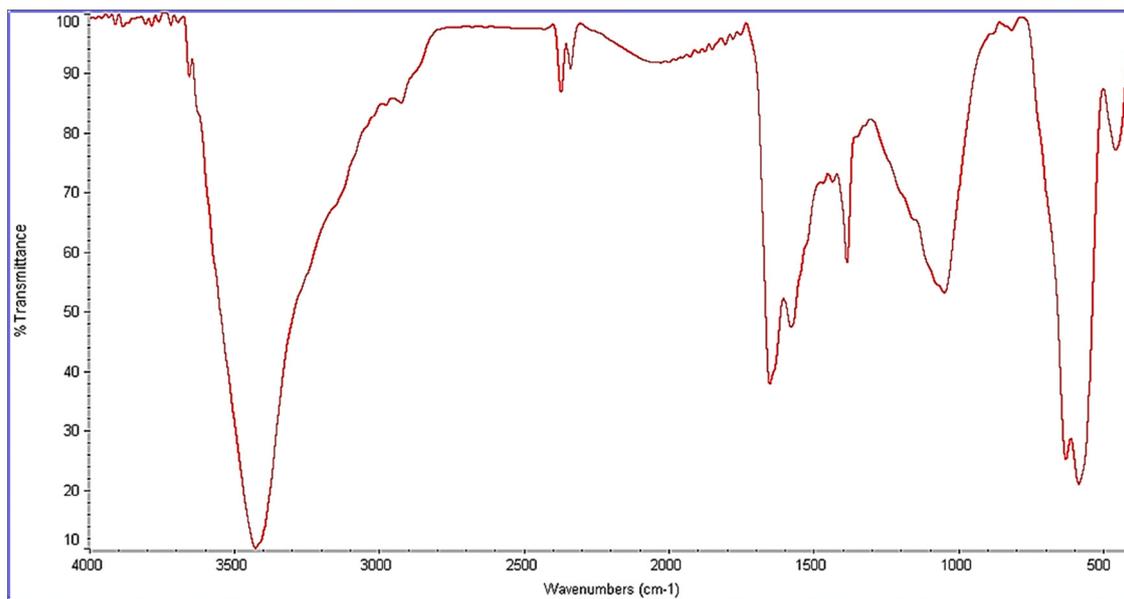
Fig. 11 FT-IR spectrum of the recovered Gu-GO/Fe$_3$O$_4$ catalyst.

with an 85% yield, which remained notably lower than the 98% achieved using the supported Gu-GO/Fe$_3$O$_4$ catalyst. The diminished efficiency of the homogeneous system is attributed to reduced substrate–catalyst interactions, and the absence of surface-driven effects inherent to GO/Fe$_3$O$_4$ (Table 3, entry 4 *vs.* entry 15).

Following the optimization of the reaction conditions, a diverse range of aldehydes featuring both electron-donating and electron-withdrawing substituents were used in the synthesis of the corresponding polyhydroquinoline derivatives (Table 4). The reactions yielded good to excellent product yields, demonstrating the versatility of the optimized catalytic system for the preparation of these valuable compounds. These results suggest that the catalytic performance is not significantly impacted by the electronic properties of the aldehyde substrates. Heteroaromatic aldehydes also participated smoothly in the reaction, delivering the corresponding products in excellent yields. Their distinct electronic characteristics likely promote the transformation, further highlighting the efficiency and broad substrate scope of the reaction (Table 4, entries 11 and 12).

To evaluate the scalability and practical applicability of the catalytic system, a gram-scale Hantzsch reaction was performed using 4-cyanobenzaldehyde (1.00 g, 7.6 mmol), dimedone (1.06 g, 7.6 mmol), ethyl acetoacetate (0.99 g, 7.6 mmol) and ammonium acetate (0.82 g, 10.46 mmol) in the presence of Gu-GO/Fe$_3$O$_4$ as the catalyst under the optimized conditions. Remarkably,

the reaction reached completion within 10 min, furnishing the corresponding polyhydroquinoline derivative in 99% yield. This result highlights the excellent catalytic efficiency, operational simplicity, and scalability of the Gu-GO/Fe$_3$O$_4$-based system, making it a promising candidate for preparative and potentially industrial applications.

Subsequent investigation focused on the recoverability and reusability of the Gu-GO/Fe$_3$O$_4$ nanocatalyst in the four-component condensation of benzaldehyde, dimedone, ethyl acetoacetate, and ammonium acetate under the optimized reaction conditions. Upon completion of the reaction, the catalyst was magnetically separated and subsequently reused in subsequent reaction cycles. This process was repeated, demonstrating that the catalyst could be recovered and reused for at least nine cycles under the described conditions without significant loss of catalytic activity (Fig. 9). To verify the structural and chemical stability of the catalyst after nine consecutive reuse cycles, the recovered sample was subjected to SEM and FT-IR analyses. The SEM image of the reused catalyst (Fig. 10) demonstrated a morphology closely resembling that of the fresh sample, indicating that the catalyst retained its structural integrity throughout the reaction conditions. In addition, the FT-IR spectrum of the recycled material (Fig. 11) showed no significant differences compared to that of the original catalyst, confirming that the Gu-GO/Fe$_3$O$_4$ catalyst

Table 5 The comparative investigation between the performance of the present catalyst and that of other catalysts

Catalyst (amount)	Solvent	Temperature (°C)	Time (min)	Yield (%)	Recovery times	Ref.
Cu@BPMO-Ph-IL (0.45 mol%)	Solvent free	60	20	95	6	69
V–TiO$_2$ (2 mol%)	Solvent free	80	12	90	4	70
[TBA]$_2$[W$_6$O$_{19}$] (7 mol%)	Solvent free	110	20–30	95	5	71
MIL-101(Cr)@EDTA–Zn(II) (11 mg)	EtOH	Reflux	15	98	8	67
Ch-rhomboclase NCs (1.8 mol%)	Solvent free	80	60	95	7	72
Gu-GO/Fe$_3$O$_4$ (5 mg)	Solvent free	50	20	98	9	This work

remained chemically stable during the applied catalytic process.

A leaching test was performed to investigate the nature of the Gu-GO/Fe$_3$O$_4$ catalyst in the model condensation reaction involving benzaldehyde, dimedone, ethyl acetoacetate, and ammonium acetate under the optimized conditions. After allowing the reaction to proceed to approximately 50% completion, the catalyst was separated from the reaction mixture and the progress of the catalyst-free residue was monitored. Notably, no further conversion was observed after 1 h, confirming the heterogeneous character of the Gu-GO/Fe$_3$O$_4$ catalyst. This result demonstrates that the catalytic activity is inherently linked to the solid catalyst and not due to leached species, thereby validating the robustness and stability of the Gu-GO/Fe$_3$O$_4$ catalyst under the tested reaction conditions. In addition, the TLC analysis of the catalyst-free residue also proved no-leaching of active guanidine-species under the applied conditions.

A comparative study was conducted to evaluate the performance of the Gu-GO/Fe$_3$O$_4$ catalyst against various catalytic systems previously used in the synthesis of polyhydroquinolines (Table 5). The findings demonstrated that the Gu-GO/Fe$_3$O$_4$ catalyst outperformed other catalytic systems in terms of mild reaction conditions, reaction rate, and reusability. This highlights the potential of the Gu-GO/Fe$_3$O$_4$ catalyst as a more efficient and sustainable alternative for the synthesis of polyhydroquinolines. The enhanced performance can be attributed to the unique properties of the Gu-GO/Fe$_3$O$_4$ catalyst, which enable efficient catalysis under mild conditions and facilitate catalyst recovery for repeated use.

4. Conclusions

A novel guanidine-functionalized graphene oxide/Fe$_3$O$_4$ nanocomposite (Gu-GO/Fe$_3$O$_4$) was synthesized. Successful immobilization of guanidine moieties onto the GO/Fe$_3$O$_4$ nanocomposite was confirmed by FT-IR, EDX, and TGA. XRD analysis demonstrated the structural stability of the Fe$_3$O$_4$ nanoparticle crystalline phase throughout the Gu-GO/Fe$_3$O$_4$ synthesis. SEM imaging revealed the presence of spherical Fe$_3$O$_4$ NPs and the characteristic layered morphology of GO within the Gu-GO/Fe$_3$O$_4$ nanocomposite. The synthesized Gu-GO/Fe$_3$O$_4$ nanocomposite exhibited robust catalytic activity and high recoverability in the synthesis of polyhydroquinoline derivatives, affording high product yields in short reaction times under mild conditions.

Author contributions

A. R.: investigation, writing – original draft, resources, and formal analysis. A. S. B.: conceptualization, writing – review and editing, supervision, and visualization. S. A.: resources and formal analysis.

Conflicts of interest

There are no conflicts of interest to declare.

Data availability

All data and materials are included in the manuscript.

References

1 S. Ayni, M. Sabet, M. Salavati-Niasari and M. Hamadanian, *J. Mater. Sci.: Mater. Electron*, 2016, **27**, 7342–7352.

2 M. Sabet, M. Salavati-Niasari and E. Esmaeili, *J. Inorg. Organomet. Polym. Mater.*, 2016, **26**, 738–743.

3 M. Yousefi, M. Sabet, M. Salavati-Niasari and S. M. Hosseinpour-Mashkani, *J. Clust. Sci.*, 2012, **23**, 491–502.

4 M. Ghanbari, M. Sabet and M. Salavati-Niasari, *J. Mater. Sci.: Mater. Electron.*, 2016, **27**, 11092–11101.

5 M. Ebadi, O. Amiri and M. Sabet, *Sep. Purif. Technol.*, 2018, **190**, 117–122.

6 A. A. Musa, A. Bello, S. M. Adams, A. P. Onwualu, V. C. Anye, K. A. Bello and I. I. Obianyo, *Polymers*, 2025, **17**, 893.

7 N. Baig, I. Kammakakam and W. Falath, *Mater. Adv.*, 2021, **2**, 1821–1871.

8 N. Sharma, H. Ojha, A. Bharadwaj, D. P. Pathak and R. K. Sharma, *RSC adv.*, 2015, **5**, 53381–53403.

9 V. Polshettiwar and R. S. Varma, *Green Chem.*, 2010, **12**, 743–754.

10 V. S. Padalkar, V. D. Gupta, K. R. Phatangare, V. S. Patil, P. G. Umape and N. Sekar, *Green Chem. Lett. Rev.*, 2012, **5**, 139–145.

11 M. Miceli, P. Frontera, A. Macario and A. Malara, *Catalysts*, 2021, **11**, 591.

12 A. Barzkar and A. S. Beni, *Sci. Rep.*, 2023, **13**, 10336.

13 A. Barzkar, A. Salimi Beni, S. Parang and F. Salahshour, *Sci. Rep.*, 2023, **13**, 19940.

14 M. Yazdani, D. Elhamifar and M. Shaker, *J. Inorg. Organomet. Polym. Mater.*, 2025, 1–16.

15 S. Sharma, P. Sharma, D. Das, V. K. Vashistha, J. Dhiman, R. Sharma, R. Kumar, M. Vir Singh and Y. Kumar, *Heliyon*, 2024, **10**, e40451.

16 S. Sharma, B. Suman and V. Kaith, *ChemistrySelect*, 2024, **9**, e202401627.

17 S. Sharma, K. Bhatrola, A. Irfan, N. Devi, K. Mishra, K. Dubey, A. Mittal, E. Mateev and V. K. Vashistha, *Tetrahedron*, 2024, **167**, 134246.

18 Vaishali, S. Sharma, E. Alwan, N. Verma, S. Johari, L. Zaharani, S. A. Salami, Rachna, N. Rani and S. Rani, *Monatsh. Chem.*, 2025, **156**, 247–277.

19 S. Sharma, Vaishali, A. Pandey, A. Garg, P. Sharma, K. Bhatrola, A. Irfan, N. Devi, L. Rubab, K. Mishra, K. Dubey and E. Mateev, *J. Heterocycl. Chem.*, 2025, **62**, 164–191.

20 X. Fan, G. Zhang and F. Zhang, *Chem. Soc. Rev.*, 2015, **44**, 3023–3035.

21 N. M. Julkapli and S. Bagheri, *Int. J. Hydrogen Energy*, 2015, **40**, 948–979.

22 E. Pérez-Mayoral, V. Calvino-Casilda and E. Soriano, *Catal. Sci. Technol.*, 2016, **6**, 1265–1291.

23 A. Bahuguna, A. Kumar and V. Krishnan, *Asian J. Org. Chem.*, 2019, **8**, 1263–1305.

24 Y. Cheng, Y. Fan, Y. Pei and M. Qiao, *Catal. Sci. Technol.*, 2015, **5**, 3903–3916.

25 S. Gupta, R. Banu, C. Ameta, R. Ameta and P. B. Punjabi, *Top. Curr. Chem.*, 2019, **377**, 1–62.

26 S. Perveen, R. Nadeem, M. Iqbal, S. Bibi, R. Gill, R. Saeed, S. Noreen, K. Akhtar, T. M. Ansari and N. Alfryyan, *J. Mol. Liq.*, 2021, **339**, 116746.

27 M. Alboghbeish, A. Larki and S. J. Saghanezhad, *Sci. Rep.*, 2022, **12**, 9658.

28 P. Moradi and M. Hajjami, *RSC Adv.*, 2021, **11**, 25867–25879.

29 F. Dadvar and D. Elhamifar, *Sci. Rep.*, 2023, **13**, 19354.

30 F. Dadvar and D. Elhamifar, *Nanoscale Adv.*, 2024, **6**, 5398–5408.

31 A. Banaei, A. Saadat, R. Javadi and P. Pargolghasemi, *Sci. Rep.*, 2024, **14**, 15457.

32 E. M. Pérez-Rodriguez, N. Gutierrez-Niño, N. Santos-Santos, R. Cabanzo-Hernandez and E. Mejia-Ospino, *Emergent Mater.*, 2024, **7**, 1953–1960.

33 N. A. Zubir, C. Yacou, J. Motuzas, X. Zhang and J. C. Diniz da Costa, *Sci. Rep.*, 2014, **4**, 4594.

34 E. Doustkhah and S. Rostamnia, *J. Colloid Interface Sci.*, 2016, **478**, 280–287.

35 G. He, W. Liu, X. Sun, Q. Chen, X. Wang and H. Chen, *Mater. Res. Bull.*, 2013, **48**, 1885–1890.

36 J. Hu, Y.-L. Dong, X.-J. Chen, H.-J. Zhang, J.-M. Zheng, Q. Wang and X.-G. Chen, *Chem. Eng. J.*, 2014, **236**, 1–8.

37 G. Peng, M. Zhang, S. Deng, D. Shan, Q. He and G. Yu, *Chem. Eng. J.*, 2018, **341**, 361–370.

38 S. M. Haghighi, A. Hemmati, H. Moghadamzadeh, A. Ghaemi and N. Raoofi, *Sci. Rep.*, 2024, **14**, 14386.

39 H. Veisi, T. Tamoradi, A. Rashtiani, S. Hemmati and B. Karmakar, *J. Ind. Eng. Chem.*, 2020, **90**, 379–388.

40 P. Gupta, C. Garkoti, J. Shabir, Surabhi, D. Sah and S. Mozumdar, *Res. Chem. Intermed.*, 2021, **47**, 4013–4028.

41 M. Shaker and A. S. Beni, *J. Porous Mater.*, 2021, **28**, 435–449.

42 E. Rahmati and Z. Rafiee, *Sci. Rep.*, 2023, **13**, 9517.

43 Q. Zhang, X.-M. Ma, H.-X. Wei, X. Zhao and J. Luo, *RSC adv.*, 2017, **7**, 53861–53870.

44 M. Mousapour and F. Shirini, *ChemistrySelect*, 2021, **6**, 4247–4255.

45 P. Choudhury, P. Ghosh and B. Basu, *Mol. Divers.*, 2020, **24**, 283–294.

46 S. M. Ramish, A. Ghorbani-Choghamarani and M. Mohammadi, *Sci. Rep.*, 2022, **12**, 1479.

47 S. Rostamnia and A. Morsali, *RSC adv.*, 2014, **4**, 10514–10518.

48 J. Safari and Z. Zarnegar, *RSC adv.*, 2013, **3**, 26094–26101.

49 A. Allahresani, M. Mohammadpour Sangani and M. A. Nasseri, *Appl. Organomet. Chem.*, 2020, **34**, e5759.

50 M. Faizan, R. Kumar, A. Mazumder, Salahuddin, N. Kukreti, P. K. Tyagi and B. Kapoor, *Synth. Commun.*, 2024, **54**, 1221–1244.

51 A. Kumar and R. A. Maurya, *Tetrahedron*, 2007, **63**, 1946–1952.

52 S. Mondal, B. C. Patra and A. Bhaumik, *ChemCatChem*, 2017, **9**, 1469–1475.

53 S. Jadhvar, H. Kasraliker, S. Goswami, A. Chakrawar and S. Bhusare, *Res. Chem. Intermed.*, 2017, **43**, 7211–7221.

54 V. Kumar, K. Singh, S. Sharma, D. Singh, C. C. Malakar and V. Singh, *Org. Biomol. Chem.*, 2025, **23**, 4782–4793.

55 V. Kumar, S. Sharma, Vaishali, D. Singh, C. C. Malakar and V. Singh, *Eur. J. Org. Chem.*, 2024, e202400456.

56 V. Kumar, S. Sharma, S. Kumar Pandey and V. Singh, *Eur. J. Org. Chem.*, 2024, e202400582.

57 V. Kumar, J. Panchal, V. Sharma, S. Sharma, P. Sharma and V. Singh, *Org. Biomol. Chem.*, 2025, **23**, 900–907.

58 F. Guodong, G. Mingming, L. Qi, M. Hongyu, L. Guanghua, M. Qiang, F. Qiang, H. Yanfu and S. Zhiguang, *New J. Chem.*, 2016, **40**, 8444–8450.

59 M. Heidarizadeh, E. Doustkhah, S. Rostamnia, P. F. Rezaei, F. D. Harzevili and B. Zeynizadeh, *Int. J. Biol. Macromol.*, 2017, **101**, 696–702.

60 F. Moniriyan, S. J. Sabounchei, A. Yousefi and O. Akhavan, *J. Nanoparticle Res.*, 2021, **23**, 192.

61 R. Eivazzadeh-Keihan, R. Taheri-Ledari, N. Khosropour, S. Dalvand, A. Maleki, S. M. Mousavi-Khoshdel and H. Sohrabi, *Colloids Surf. A: Physicochem. Eng. Asp.*, 2020, **587**, 124335.

62 N. Esmaeili, P. Mohammadi, M. Abbaszadeh and H. Sheibani, *Int. J. Hydrog. Energy*, 2019, **44**, 23002–23009.

63 H. Jin and J. Dong, *Colloids Surf. A: Physicochem. Eng. Asp.*, 2019, **581**, 123803.

64 M. P. da Silva, A. C. A. de Souza, Á. R. D. Ferreira, P. L. A. do Nascimento, T. J. M. Fraga, J. V. F. L. Cavalcanti, M. G. Ghislandi and M. A. da Motta Sobrinho, *Sci. Rep.*, 2024, **14**, 18916.

65 R. Klaewkla, M. Arend and W. F. Hoelderich, *A review of mass transfer controlling the reaction rate in heterogeneous catalytic systems*, INTECH Open Access Publisher London, UK, 2011.

66 M. Himaja, D. Poppy and K. Asif, *Int. J. Res. Ayurveda Pharm.*, 2011, **2**, 1079–1086.

67 A. Nikseresht, F. Ghoochi and M. Mohammadi, *ACS Omega*, 2024, **9**, 28114–28128.

68 J. Rakhtshah, S. Salehzadeh, M. A. Zolfigol and S. Baghery, *J. Coord. Chem.*, 2017, **70**, 340–360.

69 D. Elhamifar and H. Ardeshirfard, *J. Colloid Interface Sci.*, 2017, **505**, 1177–1184.

70 G. D. Rao, S. Nagakalyan and G. Prasad, *RSC adv.*, 2017, **7**, 3611–3616.

71 A. Davoodnia, M. Khashi and N. Tavakoli-Hoseini, *Chin. J. Catal.*, 2013, **34**, 1173–1178.

72 P. Kamalzare, B. Mirza and S. Soleimani-Amiri, *J. Nanostructure Chem.*, 2021, **11**, 229–243.